Modeling of High-Efficiency Nonsalient Pole Transmitter in High-Power Dynamic Wireless Charging System for Electric Vehicles

Fandan Zhao, Shumei Cui, Ching Chuen Chan, *Life Fellow, IEEE*, and Chunbo Zhu, *Member, IEEE*

***Abstract*—In high-power dynamic wireless charging applications, the bipolar magnetic coupler is continuously developed due to its strong coupling ability. The latest proposed bipolar-non-salient-pole (BNSP) transmitter has shown significant improvements in performance, cost, and modularization. In this article, the efficiency of BNSP transmitter is further analyzed. A quantitative loss model is proposed to reduce the dependence of analysis on finite element simulation. The model of winding loss based on squared magnetic field analysis is introduced, and a concept of flat Litz winding design suitable for BNSP transmitter is proposed, which has lower loss and fewer nonideal loss factors. The model of core loss is established by the magnetic circuit model of BNSP transmitter and Steinmetz formula of the core material. In the experiment of 40 kW power, the proposed loss model is verified to describe loss components in BNSP transmitter accurately. Compared with bipolar-salient-pole transmitter of the same power level, BNSP transmitter is quite smaller in size and more compact in structure, with 28.2% shorter Litz wire and 27.6% smaller volume of cores. The rated efficiency of BNSP transmitter is 97.9%, and the dynamic efficiency of the magnetic coupler with BNSP transmitter is 94.4%–96.3%.**

***Index Terms*—Bipolar transmitter, dynamic wireless power transfer (WPT), electric vehicle (EV), high efficiency, nonsalient pole.**

I. Introduction

DYNAMIC wireless power transfer (DWPT) technology for electric vehicles provides a charging method that integrates the charging process into daily use with the feature that the transmitter is buried under the public road and the power is supplied to any driving vehicle loaded with the matching receiver. This charging method not only greatly improves the portability but also significantly reduces the energy storage needs of electric vehicles [1], [2]. With the continuous development of DWPT technology and the implementation of industrialization attempts, the future DWPT system needs to be able to supply higher power for vehicles with higher speeds [3], [4], [5].

Since the power supply segment contains a resonant topology with certain startup and response time [6], [7], the larger the power capacity of the power supply segment with larger rated current and power demand, the more difficult it is to reduce the switching time of the power supply segment. Although the design of a longer segment or control strategy of starting in advance can alleviate this contradiction [8], [9], it will sacrifice the overall efficiency of the system. Therefore, as the largest and most critical component of energy storage and exchange in the future high-power DWPT system of electric vehicles, the coupler is required higher efficiency.

In the high-power DWPT system, the transmitter is required to have larger power capability than the receiver for charging multiple vehicles or interoperating with different receivers [10], [11]. Therefore, the transmitter is usually the research focus of the magnetic coupler. The transmitter can be divided into coil-array type and long-track type based on the shape [12], or into unipolar type and bipolar type based on the coupling principle [13]. It can be found that the bipolar type has advantages in coupling ability, misalignment tolerance, and magnetic leakage.

Considering the bipolar type of different shapes, the coil-array type is developed from static wireless power transfer (SWPT) systems [14], [15], [16], so it is easy to achieve interoperability according to SWPT standard. In landmark research, a bipolar coil-array transmitter with 10 kW power was proposed [17]. However, the extensive use of wires in limited space will lead to difficulties in achieving higher power capacity, and wide transmitter will require large modification area of the road.

The bipolar long-track type was initially developed in DWPT applications for electric bus. In landmark research, the transmission power exceeded 20 kW, but the width of the transmitter was only 10 cm, implying small modification area of the road [18]. A series of analysis and optimization designs was conducted to improve performance [12], [19], [20]. But a large amount of magnetic core may cause difficulties in achieving higher power capacity. Recently, a bipolar-non-salient pole (BNSP) transmitter has been proposed, which has shown significant progress in coupling ability, overall size, application cost, and deployment [21]. Due to that BNSP transmitter is similar to other so-called bipolar-salient pole (BSP) transmitters in principle, the model research of BNSP transmitter has important reference value for BSP transmitter.

Manuscript received 27 December 2022; revised 4 May 2023 and 29 July 2023; accepted 24 September 2023. Date of publication 2 October 2023; date of current version 16 May 2024. This work was supported by the National Natural Science Foundation of China under Grant 52177003. Recommended for publication by Associate Editor G. A. Covic. *(Corresponding author: Chunbo Zhu.)*

The authors are with the School of Electrical Engineering and Automation, Harbin Institute of Technology, Harbin 150080, China and also with the Zhengzhou Research Institute, Harbin Institute of Technology, Harbin 150080, China (e-mail: zhaofandan_hit@126.com; cuism@hit.edu.cn; ccchan@eee.hku.hk; zhuchunbo@hit.edu.cn).

Color versions of one or more figures in this article are available at https://doi.org/10.1109/TPEL.2023.3321154.

Digital Object Identifier 10.1109/TPEL.2023.3321154

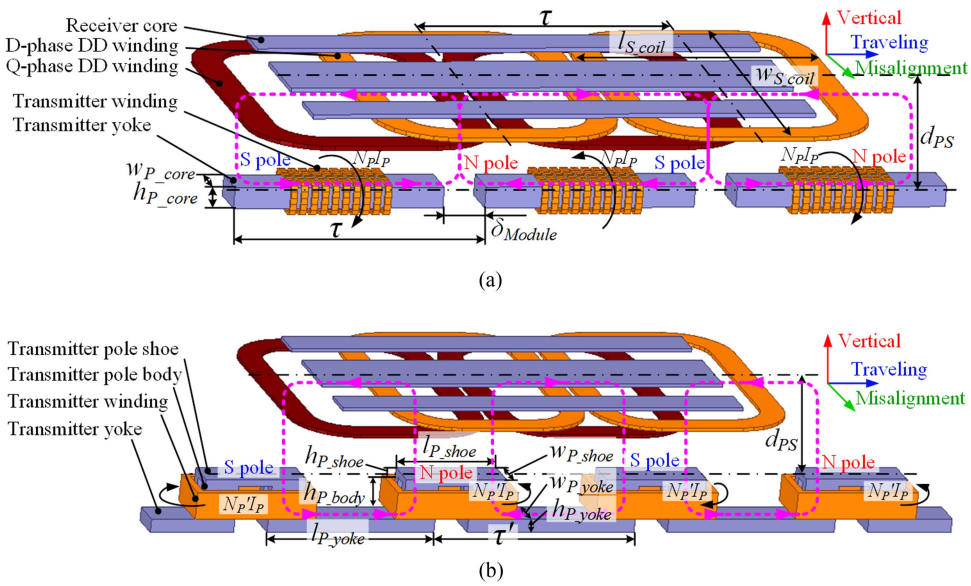

Fig. 1. Principle of a coupler with (a) BNSP transmitter and (b) BSP transmitter.

The loss calculation of transmitter or receiver of a DWPT system is a bit more special than other magnetic components due to irregular shape, large magnetic leakage, and Litz-wire winding. Since power transmitting relies on the resonant coupling of magnetic field, researches of transmission efficiency generally include the loss of resonant topology, and then the loss of coupler is generally expressed by equivalent resistance to simplify the analysis [22], [23], [24], [25]. In fact, due to the different core-loss characteristics from resistance, this analysis method is only suitable for couplers with a relatively small amount of magnetic core. The most accurate method is based on the electromagnetic field equation, where the magnetic field distribution generated by each micro conductor of coupler is calculated, and then the result is integrated to obtain overall inductance and loss [26], [27]. However, the computational workload and the difficulty of manually implementing this method are relatively large. The most widely used method is finite element simulation [28], which can obtain the loss of any coupler without manual calculation. In [29], a method based on squared field analysis was further proposed to predict winding loss, where Litz wire can be equivalent to solid wire in the finite element simulation of magnetic field. It helps to quickly analyze or compare the loss characteristic of different winding designs. However, when calculating core loss, finite element simulation is heavily relied on due to the lack of analytical model. In the preliminary design or optimization stage of a magnetic coupler, a large amount of scanning is required to obtain the relationship between parameters and loss characteristics, and the computational workload increases exponentially with more parameters and optimization objectives.

In this article, BNSP transmitter is selected as the analysis object with less reliance on finite element simulation in a high-power DWPT system. The method based on squared magnetic field analysis is introduced to establish the loss model of Litz-wire winding in BNSP transmitter, and the reduction of winding loss is discussed according to the comparison of calculated and measured results. The model of magnetic flux inside the core of BNSP transmitter is established according to the magnetic circuit division method, then the model of core loss is obtained by inputting Steinmetz formula of the core material. In the experiment, BNSP transmitter for 40 kW DWPT system is produced and the loss is measured to verify the loss model. In addition, the performance advantages of BNSP transmitter are verified by comparative experiments with existing BSP transmitter.

II. Analysis of Basic Principle

The principle of a coupler with BNSP transmitter or BSP transmitter is shown in Fig. 1. Design parameters of the coupler are shown in Table I. Since the receiver is not analysis object, a two-phase double-D (DD) receiver [30], which matches general BNP transmitter is chosen to match BNSP transmitter. Structures of pole shoe and pole body in BNP transmitter are omitted in BNSP transmitter, which significantly reduces the size and cost of BNSP transmitter. The transmitter is composed of multiple modules with windings of adjacent modules wound in opposite directions. Therefore, the magnetic pole distribution of alternating N pole and S pole, which is typical in bipolar transmitter, is generated between modules. In order to obtain all three coupling loops between BNSP transmitter and DD receiver, as shown in Fig. 1, the minimum length of BNSP transmitter is 3τ, and that of any other bipolar transmitter is 4τ [14], [21]. It means when transmitting power and switching speed of segments meet the requirements, higher power density, average dynamic efficiency, and lower magnetic leakage can be achieved by BNSP transmitter with shorter segment length.

The principle of DWPT system with BNSP transmitter is shown in Fig. 2. It is assumed that the vehicle with receiver travels along power supply segments at constant speed v_0, and

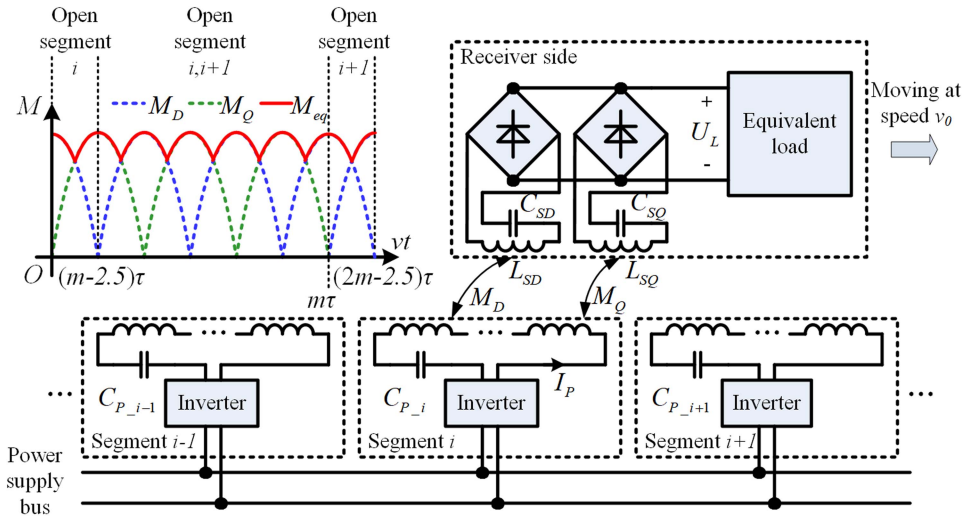

Fig. 2. Principle of DWPT system with BNSP transmitter (*m=3* in the example).

TABLE I
DESIGN PARAMETERS OF THE COUPLER

Object	Parameter	Symbol	Value
BNSP transmitter	Pole distance	τ	600 mm
	Width of transmitter yoke	w_{P_core}	100 mm
	Height of transmitter yoke	h_{P_core}	50 mm
	Length of module gap	δ_{Module}	50 mm
	Turns of transmitter winding	N_P	10
BSP transmitter	Pole distance	τ'	600 mm
	Length of pole shoe	l_{P_shoe}	300 mm
	Width of pole shoe	w_{P_shoe}	100 mm
	Height of pole shoe	h_{P_shoe}	20 mm
	Height of pole body	h_{P_body}	100 mm
	Length of transmitter yoke	l_{P_yoke}	500 mm
	Width of transmitter yoke	w_{P_yoke}	100 mm
	Height of transmitter yoke	h_{P_yoke}	40 mm
	Turns of transmitter winding	N_P'	6
	Rated current of transmitter	I_P	120 A (rms)
	Resonant frequency	f_S	20 kHz
	Transmission distance	d_{PS}	200 mm
Two-phase DD receiver	Length of receiver winding	l_{S_coil}	590 mm
	Width of receiver winding	w_{S_coil}	800 mm
	Turns of receiver winding	N_S	8

each segment contains *m* BNSP modules. Both transmitter and receiver sides adopt series resonance compensation topology. Root mean square (RMS) current and the frequency of working segments are controlled constant, and there is no phase deviation between adjacent working segments. The dynamic mutual inductance characteristic is also shown in the figure. The load voltage obtained by two-phase DD receiver is calculated by

$$\begin{aligned} U_L &= \omega_0 I_P k_{\mathrm{dc-ac}} \max(|M_D|, |M_Q|) \\ &= \frac{\pi}{2\sqrt{2}} \omega_0 I_P \max(|M_D|, |M_Q|). \end{aligned} \tag{1}$$

In (1), $k_{\mathrm{dc-ac}}$ is the gain from the average voltage of dc side to rms voltage of ac side in a rectifier [31]. Due to the inherent coefficient of fluctuation in the output of two-phase DD receiver [30], (1) can also be written as

$$U_L = \frac{\pi}{2\sqrt{2}} \omega_0 I_P M_{\mathrm{peak}} k\left(v_0 t\right), k\left(v_0 t\right) \in [1 - k_{2-\mathrm{phase}}, 1]. \tag{2}$$

In (2), M_{peak} is the maximum value of dynamic mutual inductance.

According to the analysis abovementioned, it can be assumed that the loss of a working BNSP transmitter module is a stable value P_{Pm}, and the loss of the receiver can be defined as $P_S(P_L,k(v_0t))$, which is only related to load power and the characteristic of dynamic mutual inductance.

Under ideal conditions, the startup time of each power supply segment is ignored, and the control strategy of segments is starting the next segment in advance to ensure obtaining all three coupling loops. Combined with operation modes of segments shown in Fig. 2, it can be seen that the durations of opening one segment and opening two segments are

$$\begin{cases} t_{\mathrm{single}} = \frac{(m-2.5)\tau}{v_0} \\ t_{\mathrm{dual}} = \frac{2.5\tau}{v_0} \end{cases}. \tag{3}$$

According to the abovementioned calculation, the average efficiency of the coupler in the dynamic process is

$$\begin{aligned} \eta_{av} &= \frac{P_L}{P_L + \frac{E_{\mathrm{loss}}}{t_{\mathrm{all}}}} \\ &= \frac{P_L}{P_L + (m+2.5) P_{Pm} + \frac{1}{\tau} \int_0^{\tau} P_S\left(P_L, k\left(x\right)\right) dx}. \end{aligned} \tag{4}$$

It can be seen in the equation that the average dynamic efficiency of the coupler is not related to *v*. During dynamic power supply, the load power can be maintained at the rated value by secondary control. Therefore, it is easy to know that the average dynamic efficiency increase with fewer modules,

and that the maximum and the minimum efficiency are obtained, respectively, at the peak point and the valley point of coupling. The average dynamic efficiency can also be evaluated by the efficiency at the peak point and the valley point for convenience.

Ignoring the influence from the external environment, the loss of BNSP transmitter is divided into winding loss and core loss as follows:

$$P_P = P_{P\_\text{winding}} + P_{P\_\text{core}}. \tag{5}$$

The analysis and the modeling calculation of winding loss and core loss are carried out in the following two chapters, respectively.

III. Modeling of Winding Loss

In the design of coupler for a DWPT system, the windings are usually wound by Litz wire to suppress the skin effect of high-frequency current. A large number of mutually insulated thin wires are twisted in a certain process in Litz wire to eliminate the difference of eddy-current effect between any two strands. Therefore, the current-carrying distribution of each strand can be the same under the suitable condition [32], [33]. The loss analysis of ideal Litz-wire winding is based on this assumption. The loss is divided into conduction loss and induction loss according to the principle, where the induction loss includes internal induction loss and external induction loss in further discussion [29]. The loss model is expressed as

$$\begin{cases} P_{P\_\text{winding}} = P_{Cond} + P_{Ind} \\ P_{Cond} = \frac{\xi l_{\text{Wire}} \Phi_{Cond} I^2}{2\pi r_s n_0 \sigma} \\ P_{Ind} = \frac{-4n_0\pi\xi r_s \Phi_{Ind}}{\sigma} \frac{1}{S_{\text{Wire}}} \int\limits_{V_{\text{Wire}}} H_{\text{Wire}}^2 dv \\ \quad = \frac{-4n_0\pi\xi r_s \Phi_{Ind}}{\sigma} \frac{1}{S_{\text{Wire}}} \int\limits_{V_{\text{Wire}}} \left(H_{\text{In}}^2 + H_{Ex}^2\right) dv \\ \Phi_{Cond} = \frac{ber(\xi r_s)bei'(\xi r_s) - ber'(\xi r_s)bei(\xi r_s)}{ber'^2(\xi r_s) + bei'^2(\xi r_s)} \\ \Phi_{Ind} = \frac{ber_2(\xi r_s)ber'(\xi r_s) + bei_2(\xi r_s)bei'(\xi r_s)}{ber^2(\xi r_s) + bei^2(\xi r_s)} \\ \xi = \sqrt{\mu_0 \mu_r \sigma \omega} \end{cases}. \tag{6}$$

In (6), μ_0 Is the vacuum permeability. μ_r, σ, and ω are the relative permeability, the conductivity, and the operating angular frequency of the winding, respectively. r_s and n_0 are the single-strand radius and the number of strands of Litz wire, respectively. l_{Wire}, S_{Wire}, V_{Wire}, and H_{Wire} are the length, the overall cross-sectional area, the volume, and the magnetic field intensity of the wire wound in the winding, respectively, where Litz wire can be equivalent to solid wire.

It is known that the conduction loss P_{Cond} is determined by l_{Wire}, r_s and n_0, which are difficult to adjust according to specified current and size requirements. The key to analyzing the winding loss is to calculate the integral term in (6), which is

$$IntV\left(H^2\right) = \frac{1}{S_{\text{Wire}}} \int_{V_{\text{Wire}}} H_{\text{Wire}}^2 dv. \tag{7}$$

The magnetic field intensity on each turn in the winding of BNSP transmitter, which is shown in Fig. 3, is not uniformly distributed and not suitable for simplifying to a lower dimensional model. Therefore, it is necessary to use finite-element simulation

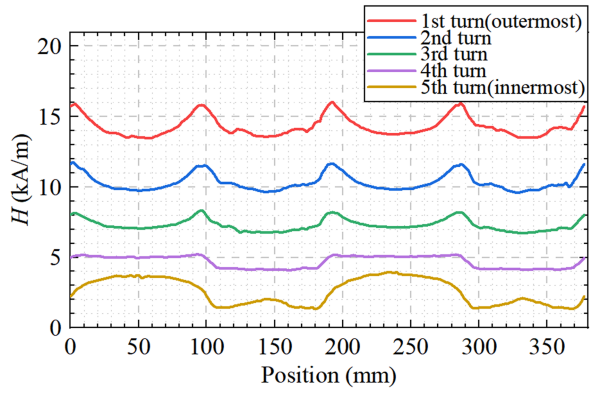

Fig. 3. Magnetic field intensity on each turn in the winding of BNSP transmitter.

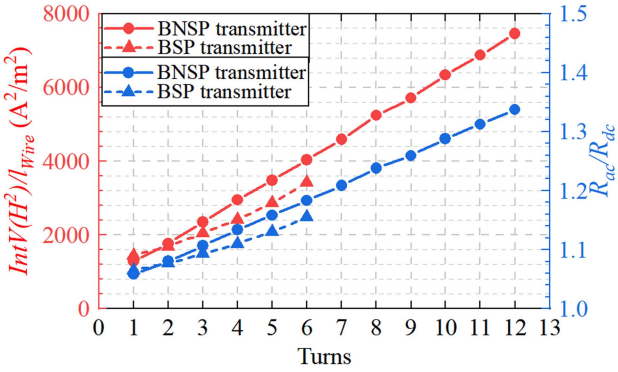

Fig. 4. Comparisons of squared field and ac resistance characteristics between BNSP and BSP transmitters.

to calculate $IntV(H^2)$, where the equivalent solid-wire winding can be used.

It can also be obtained that the more turns the winding has, the more difference in magnetic field intensity between the innermost and the outmost turn it will be, which will ultimately cause a larger ratio of ac resistance to dc resistance, namely $R_{\text{ac}}/R_{\text{dc}}$. In the comparison in [21], although the length of wire in BNSP transmitter is shorter, the turns of winding in BNSP transmitter are twice as large as that of BSP transmitter. The comparison of $IntV(H^2)$ per meter of wire and $R_{\text{ac}}/R_{\text{dc}}$ between BNSP and BSP transmitters are shown in Fig. 4. It can be seen that the growth characteristic of $R_{\text{ac}}/R_{\text{dc}}$ is similar to that of $IntV(H^2)/l_{\text{Wire}}$, and $R_{\text{ac}}/R_{\text{dc}}$ of winding in BSP transmitter is smaller than that of BNSP with double turns. To sum up, Therefore, it is of great significance to optimize the winding design to reduce $IntV(H^2)$ of the winding and the winding loss of BNSP transmitter.

In this article, flat Litz wire is introduced to replace general round Litz wire in the winding design of BNSP transmitter. The comparison of the magnetic field distribution between these two Litz-wire windings is shown in Fig. 5. The distribution of conductor is extended horizontally in flat Litz wire, so that each conductor element is affected by fewer conductors in vertical and has greater overall distance from other conductors in horizon,

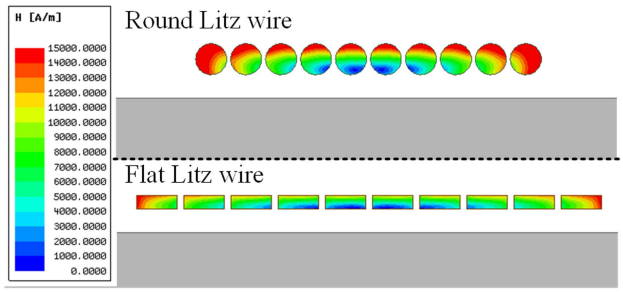

Fig. 5. Comparison of the magnetic field distribution between round Litz winding and flat Litz winding.

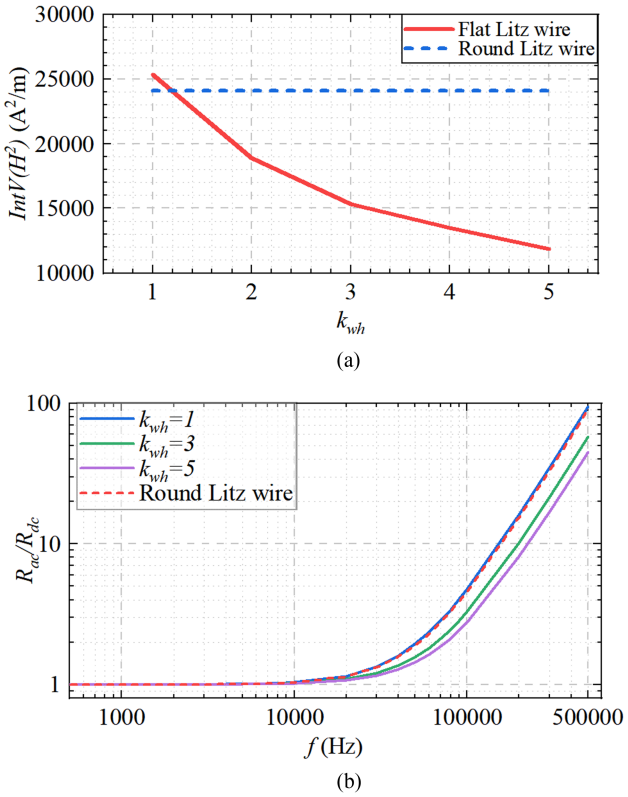

Fig. 6. Analysis of effects of width-to-thickness ratio to flat Litz winding. (a) Calculation of squared magnetic field. (b) AC resistance characteristic of different Litz wires.

which will ultimately reduce $IntV(H^2)$ of the winding. In addition, flat Litz wire has much simpler twisting structure than that of round Litz wire, which is easier to obtain the current-carrying distribution of ideal Litz wire. In practice, flat Lize wire is easier to bend, which is more suitable for winding with a small size and a large number of turns in BNSP transmitter.

The main parameter needed to discuss in the flat Litz winding design is the width-to-thickness ratio k_{wh}. The relationship between $IntV(H^2)$ and k_{wh} of flat Litz-wire winding in BNSP transmitter is shown in Fig. 6(a), and calculated curves of $R_{\rm ac}/R_{\rm dc}$ at different frequencies about round Litz winding and flat Litz windings with several values of k_{wh} are shown in Fig. 6(b) accordingly. When $k_{wh} = 1$, the $R_{\rm ac}/R_{\rm dc}$ characteristic

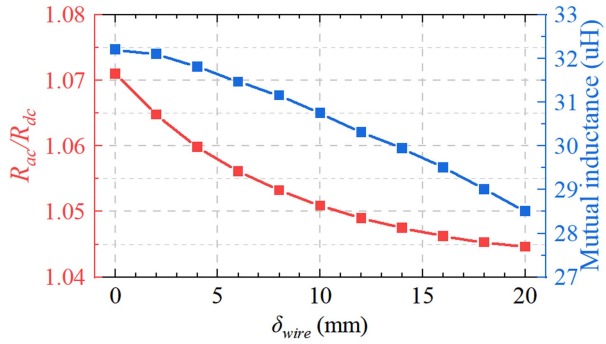

Fig. 7. Simulated results of ac resistance characteristics and mutual inductance with the distance between turns.

TABLE II
SPECIFICATIONS OF WIRES FOR COMPARISON

Type	Specification	Section size	Turns
Round Litz	0.1 mm×1500 strands	Φ 6 mm	8
Flat Litz		9×3 mm	

of Flat Litz winding is almost equal to that of round Litz winding. At 20 kHz, $R_{\rm ac}/R_{\rm dc}$ of flat Litz winding with $k_{wh} = 5$ is only 7% smaller than that with $k_{wh} = 1$. But in higher frequency, the difference is more obvious. It should be noticed that increasing the distance between turns can also reduce $R_{\rm ac}/R_{\rm dc}$ with similar principle to increasing k_{wh}. However, it may reduce the effective magnetic pole area at both ends of the yoke, and then cause attenuation in mutual inductance, as shown in Fig. 7, when flat Litz winding is already used. Therefore, both k_{wh} and the distance between turns should be designed according to the actual situation.

In practice measurement, two test windings for BNSP transmitter with round Litz wire and flat Litz wire, respectively, are made, as shown in Fig. 8(a), and the specifications of wires used are shown in Table II. Impedance analyzer E4990A is used to measure ac-resistance characteristics of these two windings, and the measured results are shown together with calculated curves in Fig. 8(b). It can be seen that the measured $R_{\rm ac}/R_{\rm dc}$ of the flat Litz winding is close to the calculated curve, while that of the round Litz winding deviates significantly from the calculated curve, especially at the frequency from 10 to 100 kHz, and the measured $R_{\rm ac}/R_{\rm dc}$ of flat Litz winding is 23.0% smaller than that of round Litz winding at the frequency of 20 kHz. The deviation is possibly caused by unsuitable twisting parameters of round Litz wire or too many bending positions, which will critically affect the twisting structure in round Litz wire.

IV. MODELING OF CORE LOSS

The coupler of DWPT system for electric vehicles is a kind of loosely coupled magnetic element with a large air gap. Although the core in the receiver will attract magnetic field nearby, it has relatively little influence on the total magnetic flux generated by the transmitter due to long transmission distance. To simplify the analysis of core loss in BNSP transmitter, two-phase DD

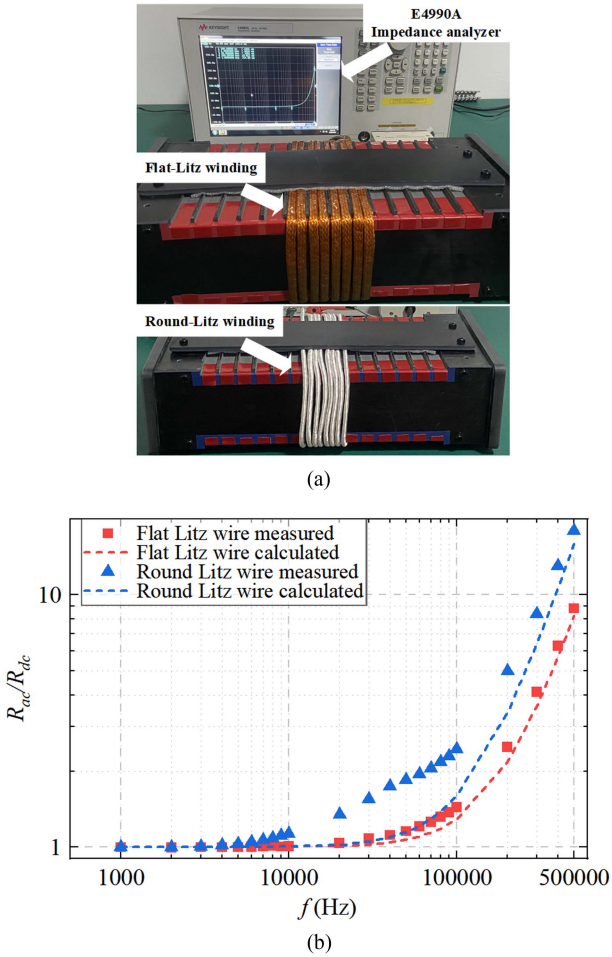

Fig. 8. Comparisons of (a) measurement of flat Litz winding and round Litz winding (b) measured and calculated results of ac resistance characteristics.

receiver is excluded. The magnetic field distribution of a four-module-BNSP transmitter on two-dimensional plane is shown in Fig. 9(a). It can be divided into several different types of flux tubes. Accordingly, the magnetic circuit model is shown in Fig. 9(b). Since the permeability of core is much greater than that of air, all magnetic resistance can be assumed to be generated by these air flux tubes. In the near region, the shapes of flux tubes A_1 and A_2 of each module are regular and similar. In the far region, the magnetic field of inner module is confined to vertical space due to the opposite direction of current in adjacent modules, and the flux tube of outer module is a bit different because of lacking confine from the one-sided adjacent module.

To calculate flux tubes in the near region accurately, a 3-D model is drawn in Fig. 10. A micro flux tube is drawn at a distance of x from the center of a module. It is known that the magnetic potential drop of the micro flux tube is

$$F(x) = \begin{cases} \frac{2\sqrt{2}xN_PI_P}{l_{\text{Winding}}} & x \in \left[0, \frac{l_{\text{Winding}}}{2}\right) \\ \sqrt{2}N_PI_P & x \in \left[\frac{l_{\text{Winding}}}{2}, \frac{\tau-\delta_{\text{Module}}}{2}\right] \end{cases}. \quad (8)$$

The average flux density of the micro flux tube can be calculated as (9) shown at the bottom of next page

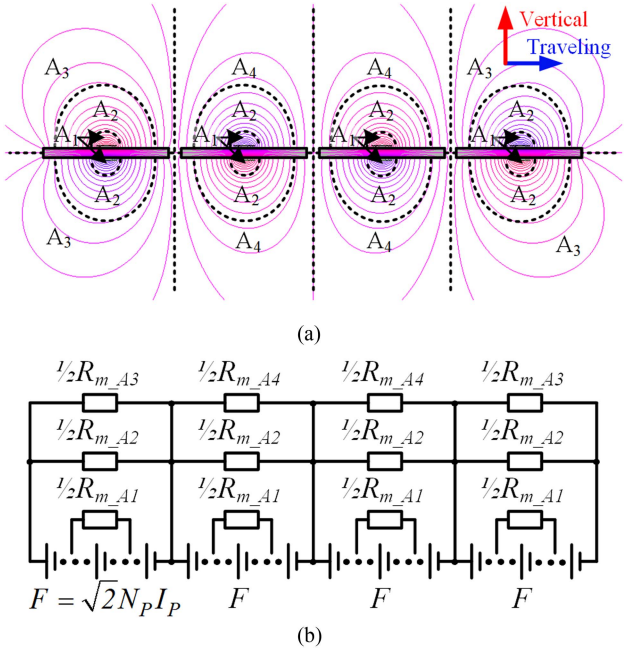

Fig. 9. Analysis of the magnetic distribution of BNSP transmitter. (a) Division of flux tubes. (b) Magnetic circuit model.

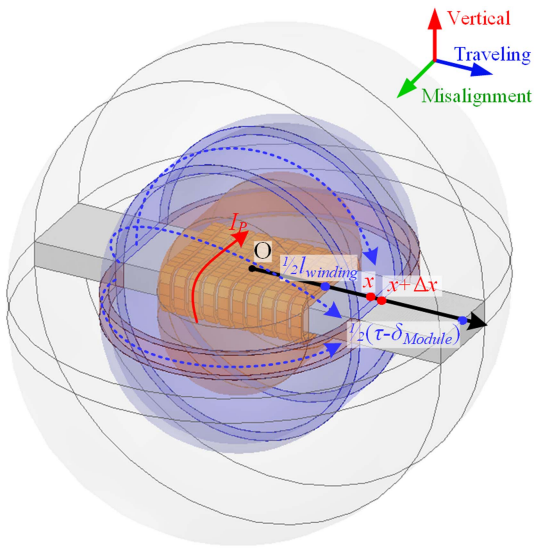

Fig. 10. Three-dimensional model of flux tubes in the near region.

The magnetic flux in the magnetic core at any position x is equal to the total flux of all flux tubes at the position from x to $l_{\text{Winding}}/2$. In addition, the magnetic flux density in the core section at any position can be considered to be uniformly distributed due to the permeability of core can be considered close to infinity. Therefore, the magnetic flux density generated by near-region flux tubes at position x in the core can be calculated as (10) shown at the bottom of next page

The magnetic flux of far-region flux tubes is difficult to calculate due to the quite irregular shape. However, it can be deduced from (9) that the magnetic flux density is as small as

close to zero at the end of the core, and largest at the center of the core. Therefore, two correction factors are introduced to consider the effect of far-region flux tubes on the magnetic flux density in the core of inner and outer modules, respectively, and the corrected magnetic flux density is expressed as

$$\begin{cases} B_{\text{CoreInner}}(x) = k_{\text{Inner}} B_{\text{Near}}(x) \\ B_{\text{CoreOuter}}(x) = k_{\text{Outer}} B_{\text{Near}}(x) \end{cases}. \tag{11}$$

The main parameters affecting the correction factors are τ, w_{P_core} and l_{Winding}, while h_{P_core} is small enough to ignore the effect. In addition, according to the magnetic circuit model, the relative size of the magnetic flux of each tube will not be affected by scaling all parameters in the same proportion. Therefore, τ is chosen as a reference, and the width factor and winding coverage factor are assumed to be

$$\begin{cases} k_w = \frac{w_{P\_\text{core}}}{\tau} \\ k_l = \frac{l_{\text{Winding}}}{\tau} \end{cases}. \tag{12}$$

The relationship between correction factors of magnetic flux density and these two factors in inner and outer modules are shown in Fig. 11. It is close to linear relation but the finer principle is more complicated. According to (10), the magnetic flux density at the center of the yoke generated by the near region flux decreases monotonously with the increase of k_l or k_w, where the change rate decreases with the increase of k_w. According to Fig. 9, k_l and k_w have no effect on the magnetic flux density at the center of the yoke generated by the far region flux, where the far region flux and its cross section in the yoke increase with the same proportion with the increase of k_w. In addition, the correction factor is negatively related to the magnetic flux density at the center of the yoke generated by the near region flux, and positively related to that generated by the far region flux. To sum up, a linear fitting model of the correction factor can be established as

$$\begin{cases} k_{\text{Inner}} = a_1 + \left(a_2 - \frac{a_3}{k_w}\right) k_l \\ k_{\text{Outer}} = b_1 + \left(b_2 - \frac{b_3}{k_w}\right) k_l \end{cases}. \tag{13}$$

The model for the inner or outer module has three undetermined coefficients, meaning that at least three simulations are required to obtain all undetermined coefficients. The fitting results with different scanning step sizes are shown in Table III, where the number of simulation times decreases exponentially as the scanning step size increases. It is proved that the characteristics within the entire parameter range can be obtained with maximum step size and minimum number of simulations.

TABLE III
FITTING RESULTS WITH DIFFERENT SCANNING STEP SIZES

Scanning range k_w k_l	Scanning step size	Fitting results a_1	a_2	a_3	b_1	b_2	b_3
[0.2, 0.5]	0.05	1.13	0.633	0.0478	1.21	0.930	0.0823
	0.15	1.13	0.633	0.0480	1.21	0.931	0.0830
	0.3	1.13	0.634	0.0492	1.20	0.932	0.0846

The calculated and simulated results of magnetic flux density in BNSP transmitter are shown in Fig. 12, where good consistency is displayed. The simulated value is a little larger than the calculated value near the end of outer module because the magnetic flux of the far-region flux tube is not confined from the other module. However, the deviation at low magnetic flux has little effect on the calculation of core loss.

The loss characteristic of the core material is obtained by measuring loss of a magnetic ring with different current at frequency from 10 to 50 kHz, and fitting all loss data to Steinmetz formula

$$P_{cv} = 0.38 f^{1.65} B_m^{2.3}. \tag{14}$$

To sum up, the core loss of BNSP transmitter with m modules can be calculated as (15) shown at the bottom of next page.

V. EXPERIMENT

The experimental platform is shown in Fig. 13, where BNSP or BSP transmitters can be adopted. The structural parameter values of BNSP transmitter and two-phase DD receiver are according to Table I, and the existing BSP transmitter is designed with same power capacity, width, and limit of magnetic flux density to BNSP transmitter. To meet the current requirement, the winding of BNSP transmitter is wound by two flat Litz wires in parallel, where the flat Litz wire is chosen in Table II. The information of the experimental platform is shown in Table IV, and the parameters of the load and compensation capacitor are adjusted accordingly to achieve the resonant state and target output power of 40 kW. It is found that BNSP transmitter is quite smaller in size and more compact in structure, with 28.2%

$$B_{\text{Flux}}(x) = \lim_{\Delta x \to 0} \frac{F(x)}{R_m(x) S(x)} = \begin{cases} \frac{2\sqrt{2}\mu_0 x N_P I_P}{l_{\text{Winding}}} \left(\frac{1}{\pi x} + \frac{1}{2w_{P\_\text{core}} + 2h_{P\_\text{core}}}\right) & x \in \left[0, \frac{l_{\text{Winding}}}{2}\right) \\ \sqrt{2}\mu_0 N_P I_P \left(\frac{1}{\pi x} + \frac{1}{2w_{P\_\text{core}} + 2h_{P\_\text{core}}}\right) & x \in \left[\frac{l_{\text{Winding}}}{2}, \frac{\tau - \delta_{\text{Module}}}{2}\right] \end{cases}. \tag{9}$$

$$\begin{aligned} B_{\text{Near}}(x) &= \int_x^{\frac{\tau-\delta_{\text{Module}}}{2}} 2B_{\text{Flux}}(r)(w_{P\_\text{core}} + h_{P\_\text{core}})\, dr \\ &= \begin{cases} \frac{2\sqrt{2}\mu_0 N_P I_P (w_{P\_\text{core}} + h_{P\_\text{core}})}{w_{P\_\text{core}} h_{P\_\text{core}}} \left(\frac{\tau - \delta_{\text{Module}} - l_{\text{Winding}}}{4w_{P\_\text{core}} + 4h_{P\_\text{core}}} + \frac{1}{\pi} \ln\left(\frac{\tau - \delta_{\text{Module}}}{l_{\text{Winding}}}\right)\right) \\ + \frac{\mu_0 N_P I_P}{w_{P\_\text{core}} h_{P\_\text{core}} l_{\text{Winding}}} \left(1 + \frac{4(w_{P\_\text{core}} + h_{P\_\text{core}})}{\pi l_{\text{Winding}}}\right) \left(\frac{l_{\text{Winding}}^2}{4} - x^2\right) & x \in \left[0, \frac{l_{\text{Winding}}}{2}\right) \\ \frac{2\sqrt{2}\mu_0 N_P I_P (w_{P\_\text{core}} + h_{P\_\text{core}})}{w_{P\_\text{core}} h_{P\_\text{core}}} \left(\frac{\tau - \delta_{\text{Module}} - 2x}{4w_{P\_\text{core}} + 4h_{P\_\text{core}}} + \frac{1}{\pi} \ln\left(\frac{\tau - \delta_{\text{Module}}}{2x}\right)\right) & x \in \left[\frac{l_{\text{Winding}}}{2}, \frac{\tau - \delta_{\text{Module}}}{2}\right] \end{cases}. \end{aligned} \tag{10}$$

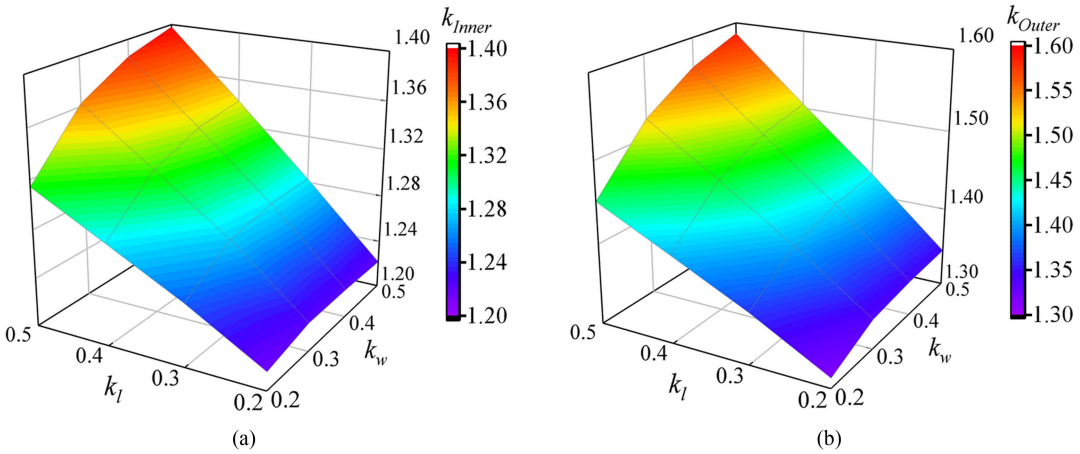

Fig. 11. Relationship between correction factors of magnetic flux density and two discussed factors in (a) inner module and (b) outer module.

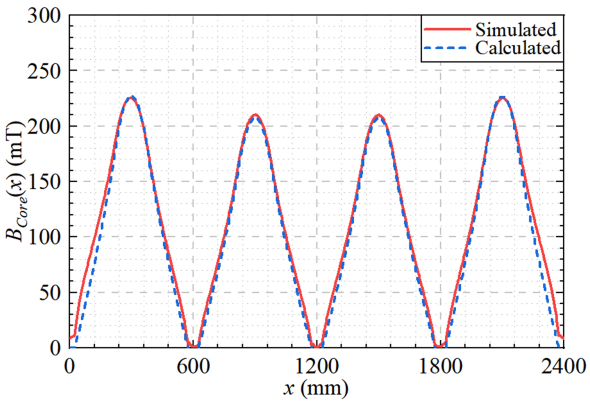

Fig. 12. Calculated and simulated results of magnetic flux density in BNSP transmitter.

TABLE IV
INFORMATION OF THE EXPERIMENTAL PLATFORM

Type of transmitter	BNSP	BSP
Resonant frequency	20 kHz	
Rated current	120 A (RMS)	
Rated output power	40 kW	
Transmission distance	200 mm	
Core width	100 mm	
Magnetic flux in the core	< 250 mT	
Outside size	600×130×70 mm (1Module)	2400×100×160 mm
Specification of wires	Flat Litz (0.1 mm×1500, 2 Parallel)	Round Litz (0.1 mm×3000)
Length of wires	17.6 m	24.5 m
Material of cores	PC95	
Volume of cores	11000 cm^3	15200 cm^3
Inductance	230 uH	230 uH

shorter Litz wire and 27.6% smaller volume of cores than BSP transmitter

The measured and the simulated results of the effective mutual inductance at different traveling distance with BNSP or BSP transmitters are shown in Fig. 14. The designed mutual inductance of BNSP and BSP transmitters is close, but smaller deviation is found between the measured and the simulated values of BNSP Transmitter. The main reason is that BNSP transmitter has much less sensitive to the gap between any two adjacent cores than BSP transmitter [21].

In power experiments, all power and losses are measured by the power analyzer PW8001. The losses of BNSP and BSP transmitters at resonant state and different current are measured and shown in Fig. 15, where the calculated loss components of BNSP transmitter, including winding loss, core loss, and additional loss from compensating capacitor and lead wires, are also displayed in the figure.

$$\begin{aligned} P_{P\_\text{core}} &= (m-2)\,P_{\text{CoreInner}} + 2P_{\text{CoreOuter}} \\ &= (2m-4)\int_0^{\frac{\tau-\delta_{\text{Module}}}{2}} 0.38 w_{P\_\text{core}} h_{P\_\text{core}} f^{1.65} B_{\text{CoreInner}}(x)^{2.3} dx \\ &\quad + 4\int_0^{\frac{\tau-\delta_{\text{Module}}}{2}} 0.38 w_{P\_\text{core}} h_{P\_\text{core}} f^{1.65} B_{\text{CoreOuter}}(x)^{2.3} dx \\ &= \left((2m-4)\,k_{\text{Inner}}^{2.3} + 4k_{\text{Outer}}^{2.3}\right)\int_0^{\frac{\tau-\delta_{\text{Module}}}{2}} 0.38 w_{P\_\text{core}} h_{P\_\text{core}} f^{1.65} B_{\text{Near}}^{2.3}(x)\,dx. \end{aligned} \tag{15}$$

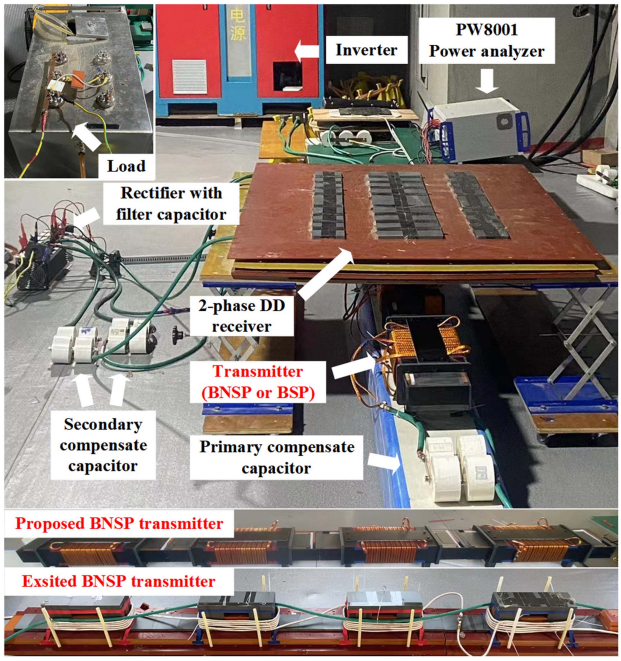

Fig. 13. Configuration of 40 kW experimental platform, where the proposed BNSP or the existed BSP transmitter can be adopted.

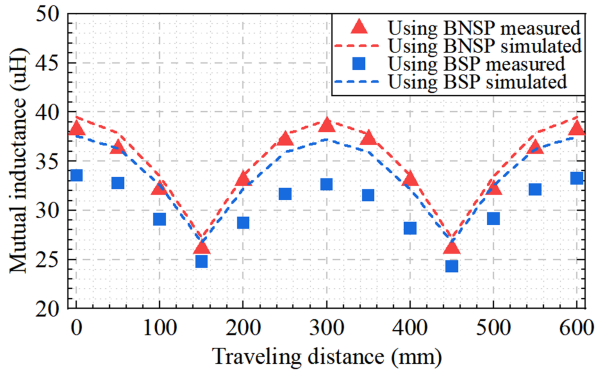

Fig. 14. Measured and simulated results of the effective mutual inductance at different traveling distance with BNSP or BSP transmitters.

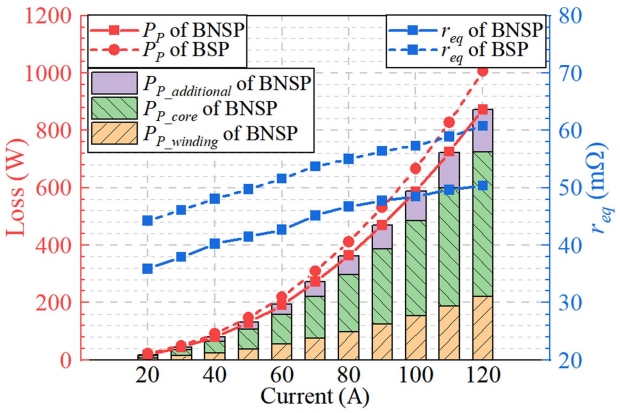

Fig. 15. Loss analysis of BNSP and BSP transmitters.

U_{rms1}	403.513 V	U_{rms1}	412.705 V
I_{rms1}	117.945 A	I_{rms1}	118.408 A
P_1	42.770 kW	P_1	43.779 kW
U_{rms2}	576.954 V	U_{rms2}	502.932 V
I_{rms2}	79.190 A	I_{rms2}	91.896 A
P_2	41.163 kW	P_2	41.660 kW
η_1	96.242 %	η_1	95.160 %
f_{l1}	19.9193 kHz	f_{l1}	19.9228 kHz
(a)		(b)	

Fig. 16. Measured power at initial position with (a) BNSP transmitter and (b) BSP transmitter.

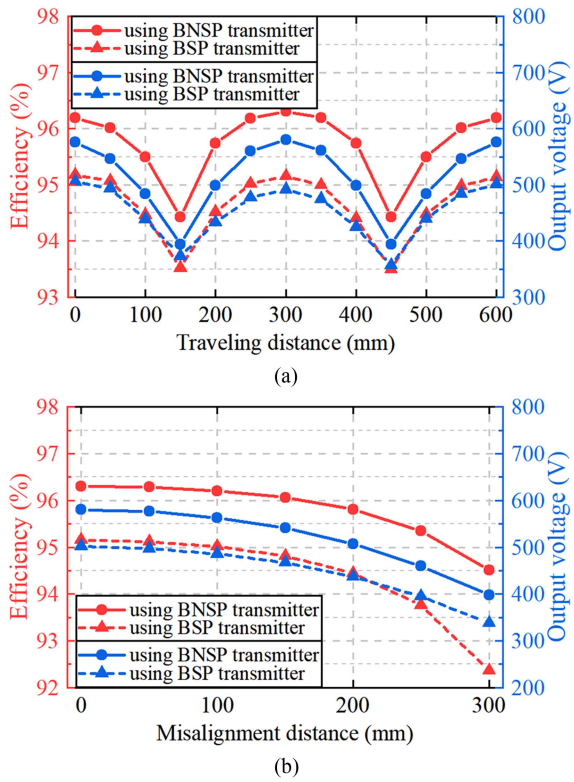

Fig. 17. Comparison of dynamic efficiency of the coupler using BNSP and BSP transmitters in (a) traveling and (b) misalignment directions.

It is found that the sum of calculated losses is in good agreement with the measured loss at any current, and the total loss (including additional loss) of BNSP transmitter is 13.3% smaller than that of BNP transmitter at rated current. It can also be deduced that the efficiency of BNSP transmitter is 97.9% in a 40 kW DWPT system. In addition, the equivalent resistances of the BNSP and BSP transmitters are also provided in the figure. The equivalent resistance of any transmitter increases by more than 30% with the current rose from 20 to 120 A. It is revealed that measured equivalent resistance under weak current

conditions cannot accurately express the actual working loss for couplers with a large amount of magnetic core.

Finally, experiments of dynamic power transmission using BNSP and BSP transmitters are carried out. The measured results at the initial position are shown in Fig. 16 and dynamic efficiency (including compensating capacitor) is shown in Fig. 17. Under the condition of no misalignment, the efficiency range of the coupler using BNSP transmitter is 94.4%–96.3%, while that of the coupler using BSP transmitter is 93.5%–95.2%. The improvement of dynamic efficiency is due to two factors. On one hand, the operating loss of BNSP transmitter is smaller than that of BSP transmitter. On the other hand, the current in DD receiver by using BNSP transmitter is smaller, which is caused by the higher coupling capability of BNSP transmitter.

VI. Conclusion

In this article, the efficiency of BNSP transmitter in the high-power DWPT system is further analyzed. A quantitative loss model of BNSP transmitter is proposed to reduce the dependence of analysis on finite element simulation. The method based on squared magnetic field analysis is introduced to calculate winding loss, and then a flat Litz winding design suitable for BNSP transmitter is proposed. The comparison of calculated and measured results between round Litz and flat Litz reveals that flat Litz is easier to bend and to obtain characteristics of ideal Litz wire. The model of magnetic flux inside the core of BNSP transmitter is established according to the magnetic circuit division method, and the flux difference between the outer module and the inner module of a power supply segment is considered. The model of core loss is obtained by combining the flux model of the core and Steinmetz formula of the core material.

In the experiment of 40 kW power, the proposed loss model is verified to describe loss components in BNSP transmitter accurately, and the performance of BNSP transmitter is compared with existing BSP transmitters under fair conditions. BNSP transmitter is quite smaller in size and more compact in structure, with 28.2% shorter Litz wire and 27.6% smaller volume of cores. The operating loss of BNSP transmitter is 13.3% smaller than that of BNP transmitter at rated current, which results in a rated efficiency of 97.9% for BNSP transmitter. The measured dynamic efficiency of the magnetic coupler with BNSP transmitter is 94.4%–96.3% and it is expected to be significantly increased along with the development of core products.

The loss model proposed in this article can be used for intelligent optimization based on algorithms, making the research and optimization of magnetic coupler more efficient. It can also provide theoretical reference for the bipolar long-track type of magnetic coupler. In the future work, analysis and calculation of magnetic shielding loss or dynamic loss will be added to further improve the quantitative loss model.

References

[1] A. Yin et al., " Analysis of battery reduction for an improved opportunistic wireless-charged electric bus," *Energies*, vol. 12, no. 15, Jul. 2019, Art. no. 2866, doi: 10.3390/en12152866.

[2] S. Jeong, Y. J. Jang, D. Kum, and M. S. Lee, "Charging automation for electric vehicles: Is a smaller battery good for the wireless charging electric vehicles?," *IEEE Trans. Automat. Sci. Eng.*, vol. 16, no. 1, pp. 486–497, Jan. 2019, doi: 10.1109/TASE.2018.2827954.

[3] Y. J. Jang, "Survey of the operation and system study on wireless charging electric vehicle systems," *Transp. Res. C, Emerg. Technol.*, vol. 95, pp. 844–866, Oct. 2018, doi: 10.1016/j.trc.2018.04.006.

[4] C. C. Mi, G. Buja, S. Y. Choi, and C. T. Rim, "Modern advances in wireless power transfer systems for roadway powered electric vehicles," *IEEE Trans. Ind. Electron.*, vol. 63, no. 10, pp. 6533–6545, Oct. 2016, doi: 10.1109/TIE.2016.2574993.

[5] S. Y. Choi, B. W. Gu, S. Y. Jeong, and C. T. Rim, "Advances in wireless power transfer systems for roadway-powered electric vehicles," *IEEE J. Emerg. Sel. Topics Power Electron.*, vol. 3, no. 1, pp. 18–36, Mar. 2015, doi: 10.1109/JESTPE.2014.2343674.

[6] S. Lee, B. Choi, and C. T. Rim, "Dynamics characterization of the inductive power transfer system for online electric vehicles by laplace phasor transform," *IEEE Trans. Power Electron.*, vol. 28, no. 12, pp. 5902–5909, Dec. 2013, doi: 10.1109/TPEL.2013.2254500.

[7] L. Chen, G. R. Nagendra, J. T. Boys, and G. A. Covic, "Double-coupled systems for IPT roadway applications," *IEEE J. Emerg. Sel. Topics Power Electron.*, vol. 3, no. 1, pp. 37–49, Mar. 2015, doi: 10.1109/JESTPE.2014.2325943.

[8] S. Li, L. Wang, Y. Guo, C. Tao, and L. Ji, "Power stabilization with double transmitting coils and T-type compensation network for dynamic wireless charging of EV," *IEEE J. Emerg. Sel. Topics Power Electron.*, vol. 8, no. 2, pp. 1801–1812, Jun. 2020, doi: 10.1109/JESTPE.2019.2915551.

[9] X.-J. Ge, Y. Sun, Z.-H. Wang, and C.-S. Tang, "Dual-independent-output inverter for dynamic wireless power transfer system," *IEEE Access*, vol. 7, pp. 107320–107333, 2019, doi: 10.1109/ACCESS.2019.2933017.

[10] R. Mai et al., " A maximum efficiency point tracking control scheme based on different cross coupling of dual-receiver inductive power transfer system," *Energies*, vol. 10, no. 2, Feb. 2017, Art. no. 217, doi: 10.3390/en10020217.

[11] K. Song et al., "Interoperability analysis and improvement for rectangular coil and DD coil of wireless EV charging," in *Proc. IEEE 22nd Int. Conf. Elect. Mach. Syst.*, 2019, pp. 1–5, doi: 10.1109/ICEMS.2019.8921949.

[12] Z. Wang et al., "A novel magnetic coupling mechanism for dynamic wireless charging system for electric vehicles," *IEEE Trans. Veh. Technol.*, vol. 67, no. 1, pp. 124–133, Jan. 2018, doi: 10.1109/TVT.2017.2776348.

[13] F. Y. Lin, G. A. Covic, and J. T. Boys, "Evaluation of magnetic pad sizes and topologies for electric vehicle charging," *IEEE Trans. Power Electron.*, vol. 30, no. 11, pp. 6391–6407, Nov. 2015, doi: 10.1109/TPEL.2015.2419592.

[14] M. G. S. Pearce, G. A. Covic, and J. T. Boys, "Reduced ferrite double D pad for roadway IPT applications," *IEEE Trans. Power Electron.*, vol. 36, no. 5, pp. 5055–5068, May 2021, doi: 10.1109/TPEL.2020.3032691.

[15] W. Chen, F. Lin, G. A. Covic, and J. T. Boys, "Design considerations of a bipolar track for dynamic electric vehicle charging," in *Proc. IEEE Energy Convers. Congr. Expo.*, 2019, pp. 1188–1194, doi: 10.1109/ECCE.2019.8912242.

[16] S. Zhou and C. Chris Mi, "Multi-paralleled LCC reactive power compensation networks and their tuning method for electric vehicle dynamic wireless charging," *IEEE Trans. Ind. Electron.*, vol. 63, no. 10, pp. 6546–6556, Oct. 2016, doi: 10.1109/TIE.2015.2512236.

[17] W. Chen, F. Lin, G. A. Covic, and J. T. Boys, "Evaluation of a meandering track primary topology for EV roadway charging," *IEEE J. Emerg. Sel. Topics Ind. Electron.*, vol. 1, no. 1, pp. 26–35, Jul. 2020, doi: 10.1109/JESTIE.2020.3004761.

[18] J. Huh, S. W. Lee, W. Y. Lee, G. H. Cho, and C. T. Rim, "Narrow-width inductive power transfer system for online electrical vehicles," *IEEE Trans. Power Electron.*, vol. 26, no. 12, pp. 3666–3679, Dec. 2011, doi: 10.1109/TPEL.2011.2160972.

[19] S. Y. Choi, S. Y. Jeong, B. W. Gu, G. C. Lim, and C. T. Rim, "Ultra-slim S-type power supply rails for roadway-powered electric vehicles," *IEEE Trans. Power Electron.*, vol. 30, no. 11, pp. 6456–6468, Nov. 2015, doi: 10.1109/TPEL.2015.2444894.

[20] B. Song, S. Cui, Y. Li, and C. Zhu, "A narrow-rail three-phase magnetic coupler with uniform output power for EV dynamic wireless charging," *IEEE Trans. Ind. Electron.*, vol. 68, no. 8, pp. 6456–6469, Aug. 2021, doi: 10.1109/TIE.2020.3005072.

[21] F. Zhao, J. Jiang, S. Cui, X. Zhou, C. Zhu, and C. C. Chan, "Research on bipolar nonsalient pole transmitter for high-power EV dynamic wireless power transfer system," *IEEE Trans. Power Electron.*, vol. 37, no. 2, pp. 2404–2412, Feb. 2022, doi: 10.1109/TPEL.2021.3105441.

[22] J. Mai, X. Zeng, Y. Yao, Y. Wang, and D. Xu, "Improved winding and compensation methods for the multilayer coil in IPT system," *IEEE Trans. Ind. Electron.*, vol. 69, no. 5, pp. 5375–5380, May 2022, doi: 10.1109/TIE.2021.3082061.

[23] A. Zakerian, S. Vaez-Zadeh, and A. Babaki, "A dynamic WPT system with high efficiency and high power factor for electric vehicles," *IEEE Trans. Power Electron.*, vol. 35, no. 7, pp. 6732–6740, Jul. 2020, doi: 10.1109/TPEL.2019.2957294.

[24] Y. Liu, R. Mai, D. Liu, Y. Li, and Z. He, "Efficiency optimization for wireless dynamic charging system with overlapped DD coil arrays," *IEEE Trans. Power Electron.*, vol. 33, no. 4, pp. 2832–2846, Apr. 2018, doi: 10.1109/TPEL.2017.2751593.

[25] Z. Zhu et al., "Efficiency optimization and power allocation of omnidirectional wireless power transfer for multiple receivers," *IEEE Trans. Ind. Electron.*, vol. 70, no. 10, pp. 9689–9699, Oct. 2023, doi: 10.1109/TIE.2022.3222593.

[26] M. Wang, J. Feng, Y. Shi, and M. Shen, "Demagnetization weakening and magnetic field concentration with ferrite core characterization for efficient wireless power transfer," *IEEE Trans. Ind. Electron.*, vol. 66, no. 3, pp. 1842–1851, Mar. 2019, doi: 10.1109/TIE.2018.2840485.

[27] Q. Deng et al., "Frequency-dependent resistance of litz-wire square solenoid coils and quality factor optimization for wireless power transfer," *IEEE Trans. Ind. Electron.*, vol. 63, no. 5, pp. 2825–2837, May 2016, doi: 10.1109/TIE.2016.2518126.

[28] M. S. A. Chowdhury and X. Liang, "Design and performance evaluation for a new power pad in electric vehicles wireless charging systems," *Can. J. Elect. Comput. Eng.*, vol. 43, no. 3, pp. 146–156, Summer 2020, doi: 10.1109/CJECE.2020.2966148.

[29] J. Liu, Q. Deng, D. Czarkowski, M. K. Kazimierczuk, H. Zhou, and W. Hu, "Frequency optimization for inductive power transfer based on AC resistance evaluation in litz-wire coil," *IEEE Trans. Power Electron.*, vol. 34, no. 3, pp. 2355–2363, Mar. 2019, doi: 10.1109/TPEL.2018.2839626.

[30] S. Cui, Z. Wang, S. Han, C. Zhu, and C. C. Chan, "Analysis and design of multiphase receiver with reduction of output fluctuation for EV dynamic wireless charging system," *IEEE Trans. Power Electron.*, vol. 34, no. 5, pp. 4112–4124, May 2019, doi: 10.1109/TPEL.2018.2859368.

[31] R. L. Steigerwald, "A comparison of half-bridge resonant converter topologies," *IEEE Trans. Power Electron.*, vol. 3, no. 2, pp. 174–182, Apr. 1988, doi: 10.1109/63.4347.

[32] J. Acero, P. J. Hernandez, J. M. Burdio, R. Alonso, and L. A. Barragdan, "Simple resistance calculation in litz-wire planar windings for induction cooking appliances," *IEEE Trans. Magn.*, vol. 41, no. 4, pp. 1280–1288, Apr. 2005, doi: 10.1109/TMAG.2005.844844.

[33] J. Acero, R. Alonso, J. M. Burdio, L. A. Barragan, and D. Puyal, "Frequency-dependent resistance in Litz-wire planar windings for domestic induction heating appliances," *IEEE Trans. Power Electron.*, vol. 21, no. 4, pp. 856–866, Jul. 2006, doi: 10.1109/TPEL.2006.876894.

Fandan Zhao was born in Jiangsu, China, in 1992. He received the B.S. and M.S. degrees in 2015 and 2017, respectively, from the School of Electrical Engineering and Automation, Harbin Institute of Technology, Harbin, China, where he is currently working toward Ph.D. degree in electrical engineering.

His research interests include magnetic coupler, resonant compensation, and system simulation of stationary and dynamic wireless power transfer for electric vehicles.

Shumei Cui was born in Heilongjiang, China, in 1964. She received the Ph.D. degree in electrical engineering from the Harbin Institute of Technology (HIT), Harbin, China, in 1998.

She was a Professor with the Department of Electrical Engineering, HIT. Her research interests include the design and control of micro and special electric machines, the electric drive system of electric vehicles, the control and simulation of hybrid electric vehicles, and intelligent test and fault diagnostics of electric machines.

Dr. Cui is a member of the Electric Vehicle Committee and the National Automotive Standardization Technical Committee. She serves as the Vice Director Member for the Micro and Special Electric Machine Committee and the Chinese Institute of Electronics.

Ching Chuen Chan (Life Fellow, IEEE) was born in 1937. He received the B.S. degree from the China University of Mining and Technology, Xuzhou, China, the M.S. degree from Tsinghua University, Beijing, China, and the Ph.D. degree from The University of Hong Kong, Hong Kong, in 1957, 1959, and 1982, respectively, all in electrical engineering.

He has more than 50 years of teaching and research experience and proposes engineering philosophy, engineering and education innovation, which laid the foundation of modern electric vehicles theory and electric vehicles electric drive theory. He has authored more than 300 papers and 11 monographs.

Dr. Chan is a Member of Chinese Academy of Engineering, Fellow of the Royal Academy of Engineering U.K., Member of Ukrainian Academy of Engineering Sciences, and Honorary Fellow of Hungarian Academy of Engineering. He is senior IET Fellow, and the former President of the Hong Kong Institution of Engineers. He was the recipient of the Toastmasters Medal by the Institution of Electrical Engineers (IEE) in 2000, "Father of Asian Electric Vehicles" by Magazine Global View in 2003, "Environmental Excellence in Transportation Award" by the Society of Automotive Engineers (SAE) in 2007, Gold Medal of Hong Kong Institution of Engineers in 2010, World Federation of Engineering (WFEO) Medal for Engineering Excellence in 2013, Prince Philip Medal of UK Royal Academy of Engineering in 2014, and "IEEE Transportation Technologies Award" by the Institute of Electrical and Electronics Engineers (IEEE) in 2018.

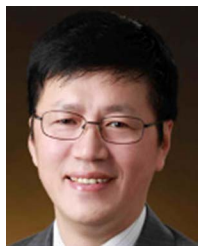

Chunbo Zhu (Member, IEEE) received the B.S. and M.S. degrees in electrical engineering and the Ph.D. degree in mechanical engineering from the Harbin Institute of Technology (HIT), Harbin, China, in 1987, 1992, and 2001, respectively.

He was a Postdoctoral Research Fellow with PEI Research Center, National University of Ireland, Galway, Ireland, from 2003 to 2004. He has been a Lecturer with the Department of Automation Measurement and Control, HIT, since 1987. He is currently a Full Professor with HIT, where he leads the Laboratory of Wireless Power Transfer and Battery Management Technologies. His current research interests include energy management systems, electric and hybrid electric vehicles, and wireless power transfer technologies.